

Sensitivity of gravity wave fluxes to interannual variations in tropical convection and zonal wind

M. Joan Alexander*

NorthWest Research Assoc.–CoRA Office, Boulder, CO, USA

David A. Ortland

NorthWest Research Assoc.—Seattle Office, Redmond, WA, USA

Alison W. Grimsdell

NorthWest Research Assoc.–CoRA Office, Boulder, CO, USA

Ji-Eun Kim

RSMAS, University of Miami, FL and JISAO, University of Washington, Seattle, WA, USA

*Corresponding author address: NorthWest Research Associates–CoRA Office, 3380 Mitchell

Lane, Boulder, CO 80301

E-mail: alexand@nwra.com

ABSTRACT

14 Using an idealized model framework with high-frequency tropical latent
15 heating variability derived from global satellite observations of precipitation
16 and clouds, we examine the properties and effects of gravity waves in the
17 lower stratosphere, contrasting conditions in an El Niño and a La Niña year.
18 The model generates a broad spectrum of tropical waves including planetary-
19 scale waves through mesoscale gravity waves. We compare modeled monthly-
20 mean regional variations in wind and temperature with reanalyses, and we val-
21 idate the modeled gravity waves using satellite- and balloon-based estimates
22 of gravity wave momentum flux. Some interesting changes in the gravity
23 spectrum of momentum flux are found in the model which are discussed in
24 terms of the interannual variations in clouds, precipitation, and large-scale
25 winds. While regional variations in clouds, precipitation, and winds are dra-
26 matic, the mean gravity wave zonal momentum fluxes entering the strato-
27 sphere differ by only 11%. The modeled intermittency in gravity wave mo-
28 mentum flux is shown to be very realistic compared to observations, and the
29 largest amplitude waves are related to significant gravity wave drag forces in
30 the lowermost stratosphere. This strong intermittency is generally absent or
31 weak in climate models due to deficiencies in parameterizations of gravity
32 wave intermittency. Our results suggest a way forward to improve model rep-
33 resentations of lowermost stratospheric quasi-biennial oscillation winds and
34 teleconnections.

35 1. Introduction

36 Long-range weather forecast skill has demonstrated links to the tropical stratosphere. The quasi-
37 biennial oscillation (QBO), a reversal of the tropical lower stratosphere zonal mean winds roughly
38 every other year, is an important source of predictability for seasonal forecasts of the North At-
39 lantic Oscillation (NAO) [Scaife et al. 2014a]. Although confined to tropical latitudes, the QBO
40 has clear connections to polar stratospheric extreme vortex events [Holton and Tan 1980] and ex-
41 tratropical surface weather conditions [Thompson et al. 2002; Garfinkel et al. 2012]. The QBO
42 also modulates the chemical composition of the stratosphere, for example dominating interannual
43 variability in tropical stratospheric water vapor with associated effects on chemistry and tempera-
44 ture [e.g. Mote et al. 1996; Randel et al. 2004].

45 The key characteristics of the QBO are zonal mean winds that oscillate from easterly to westerly
46 with an average period of 28 months. The period is inversely related to atmospheric wave mo-
47 mentum transport, or more specifically to the divergence of Eliassen-Palm flux [Dunkerton 1997],
48 which is often called wave drag or wave forcing. A range of studies have identified tropical gravity
49 waves as a crucial component of the momentum transport necessary to drive the QBO, with cur-
50 rent estimates suggesting more than half of the flux is carried by gravity waves that are generated
51 by tropical convection (e.g. Kawatani et al. [2010]). Global characterizations of gravity waves
52 and their momentum transport remain an observational challenge due to their small scales, high
53 frequencies, and intermittent occurrences [Geller et al. 2013; Alexander 2015]. Models therefore
54 play a major role in our understanding of tropical gravity waves and their effects on circulation.

55 Although the basic wave-mean flow interaction mechanism that forces the QBO has been un-
56 derstood for decades, most climate models still do not have a QBO [Schenzinger et al. 2016]. The
57 global climate and weather forecasting models that do include a QBO rely on parameterization

58 of sub-grid-scale gravity wave forcing. Such parameterizations often assume an average set of
59 wave properties, continually forced at all times and all longitudes. A few climate models include
60 varying gravity wave properties that are tied to the model’s parameterized convection (e.g. Richter
61 et al. [2014], Bushell et al. [2015]), but large uncertainties in specifying the properties of the
62 sub-gridscale gravity waves remain [Schirber et al. 2015].

63 In this study, we employ a global model that is uniquely constrained by observations in multiple
64 ways in order to examine interannual, subseasonal, and geographical variability in tropical gravity
65 waves and their effects on the stratospheric circulation. The model is designed to represent the
66 scales of gravity waves that are observed by limb-sounding satellite measurements, which provide
67 constraints for the modeled gravity wave momentum transport. Global precipitation and cloud
68 observations provide constraints on variability in latent heating that force the waves in the model.
69 Thus all the gravity waves in the model are explicitly resolved, and the tropical wave forcing
70 has observed geographical and temporal variations. Finally, zonal mean winds in the model are
71 relaxed to those in reanalysis, and the model is initialized with reanalyzed zonal mean temperatures
72 in order to realistically constrain wave propagation and interactions with the circulation.

73 In section 2, we describe the precipitation and cloud data that will be used to estimate latent
74 heating that forces tropical waves in the model. Section 3 describes the model experiment design,
75 the latent heating algorithm, and the properties of tropical clouds, precipitation, and latent heating
76 for the two experiments in El Niño and La Niña conditions. Section 4 describes the model results
77 and compares them to observations, including tropical tropopause wind and temperature varia-
78 tions, the properties of the gravity waves, and wave driving of the QBO. Section 5 is a discussion
79 of the results and their implications for global climate and weather modeling, and section 6 is a
80 summary with conclusions.

81 2. Data Description

82 *a. Background*

83 The launch of the Tropical Rainfall Measuring Mission (TRMM) satellite in 1998 began an
84 era of high-resolution global precipitation measurement. TRMM products include the TMPA
85 (3B42) gridded rain rates at $0.25^\circ \times 0.25^\circ$ spatial resolution and 3-hourly time intervals [Huff-
86 man et al. 2007]. Ryu et al. [2011] described an algorithm for computing the 3-dimensional
87 time-dependent latent heating field using TRMM 3B42 rain rates, and cloud-top height derived
88 from global merged geostationary satellite observations of infrared brightness temperatures. The
89 resulting three-dimensional time-dependent latent heating field defined sources for waves with pe-
90 riods longer than 6 hours in a dry dynamical primitive equation model. Ortland et al. [2011] used
91 this method to study the sensitivity of the wave Eliassen-Palm flux (EP-flux) spectrum to spa-
92 tial resolution in the model. They showed that at the 3-hourly temporal resolution of the TRMM
93 3B42 data, spatial resolutions resolving wavenumbers higher than 60 gave only minor increases
94 in the EP-flux. Thus for modeling gravity waves, the 3-hourly time resolution was clearly a limit-
95 ing factor. Higher-frequency gridded precipitation products available include CMORPH (Climate
96 Prediction Center morphing method) [Joyce et al. 2004] with 8-km spatial and 30-min tempo-
97 ral resolution, GSMAP (Global Satellite Mapping of Precipitation) with 0.1° spatial and 1-hourly
98 temporal resolution [Ushio et al. 2009], and a recent product called IMERG (Integrated Multi-
99 satellite Retrievals for GPM) [Huffman et al. 2015, ATBD] with 0.1° spatial and 30-min temporal
100 resolution based on new measurements from the Global Precipitation Missions (GPM). IMERG is
101 currently only available beginning in 2014, although there are plans to extend the IMERG record
102 back in time. For the present study, we seek to model the historical period 2006-2007, a time
103 when we have high-resolution satellite limb-sounding observations that we can use for validation

104 of gravity wave momentum fluxes [Alexander 2015]. We therefore utilize CMORPH rain rates
105 degraded to $0.25^\circ \times 0.25^\circ$ spatial resolution but utilizing the full 30-min temporal resolution. The
106 focus in this work will be on tropical convective wave sources within $\pm 30^\circ$ of the equator.

107 *b. CMORPH Precipitation*

108 Like other high-resolution precipitation products, CMORPH takes advantage of the frequent
109 sampling of geostationary infrared measurements and combines these with higher-quality mi-
110 crowave precipitation measurements to create a gridded spatio-temporally varying precipitation
111 rate product. Sapiano and Arkin [2009] found 3-hourly CMORPH $0.25^\circ \times 0.25^\circ$ data showed
112 the highest correlations against gauge data among several comparable data sets. However, all
113 showed a tendency to underestimate rainfall over the tropical Pacific Ocean. Habib et al. [2012]
114 evaluated CMORPH at $8 \text{ km} \times 8 \text{ km}$, 30-min resolution against dense rain gauge observations
115 and radar-based estimates in Louisiana. CMORPH was found to have negligible bias over the
116 28-day study period, high detection skills and rainfall occurrence distributions that compare very
117 well to the radar. Significant biases occurred on event scales, and missed and false-rain detections
118 were $\sim 20\%$, but these errors are reduced considerably through aggregation. Our degradation to
119 $0.25^\circ \times 0.25^\circ$ resolution partly serves that purpose, and we will further focus on statistics of wave
120 generation with a full month of data.

121 *c. Global-merged Infrared Brightness Temperature and Cloud-top Height*

122 TRMM ancillary data include global merged infrared brightness temperatures utilizing the in-
123 ternational set of geostationary measurements. The merged data is available equatorward of 60°
124 at 4-km spatial resolution and 30-min time resolution. As for the rain rate data, we degrade these
125 brightness temperatures to $0.25^\circ \times 0.25^\circ$ spatial resolution but retain the 30-min temporal reso-

lution. Occasional gaps in coverage occur but are filled by linear interpolation in time utilizing measurements in the previous and following 1.5 hours to achieve continuous coverage. A small but persistent gap in coverage occurs in the tropical Southern Hemisphere eastern Pacific, but since this is usually a dry region, it is unlikely to affect our results. Cloud-top height is estimated by matching the observed brightness temperature to regional temperature profiles taken from the MERRA reanalysis [Rienecker et al. 2011].

Figure 1 shows sample snapshots of the resulting rain rates and cloud-top heights at $0.25^\circ \times 0.25^\circ$, 30-min resolution.

3. Experiment Design

a. Latent heating

Using the precipitation rates and cloud top heights from section 2, a three-dimensional, time-dependent tropical latent heating field is calculated with the algorithm described in detail in Ryu et al. [2011]. Briefly summarizing the procedure, a combined rain-rate and cloud-height criterion categorizes the heating profile as convective or stratiform type. For the convective-type rain, heating is specified as positive everywhere with a half-sine vertical profile shape, and heating depth and peak heating are functions of rain-rate and cloud top height. For stratiform-type rain, melting level is a function of rain rate, and peak upper tropospheric heating rate and peak lower tropospheric cooling rate are functions of rain-rate and cloud height. The algorithm is similar to the TRMM Spectral Latent Heating (SLH) product [Shige et al. 2007]. In particular, it includes a factor that accounts for horizontal transport of precipitation from convective to stratiform regions.

This three-dimensional latent heating is computed at the same 30-min resolution as the cloud and precipitation data. The latent heating field can be compared to other existing latent heating

148 products after sufficient averaging. The appendix provides some additional information about the
149 latent heating.

150 *b. Model*

151 A global nonlinear spectral model is used to simulate waves forced by the space-time-varying
152 tropical latent heating. The model was described previously in Ortland et al. [2011]. There is no
153 parameterized gravity wave drag and no parameterized convection. In the present cases, the model
154 is initialized with November monthly mean zonal winds and temperatures and run for two months,
155 through the end of December. We subsequently analyze the December results only. The model
156 troposphere is forced with the three-dimensional, time-varying latent heating field, which forces
157 a broad spectrum of waves, including global-scale equatorial Rossby and Kelvin waves through
158 mesoscale gravity waves. Newtonian cooling is applied to the perturbation temperature, where a
159 perturbation is defined as the deviation from the daily MERRA zonal mean. The time scale of the
160 Newtonian cooling is 5 days in the stratosphere and 25 days in the middle and upper troposphere
161 [Ryu et al. 2011]. In the lower troposphere below 650 hPa ($\sigma > 0.7$), the Newtonian cooling time
162 scale gradually decreases to 8 days at the lowest model level [Held and Suarez 1994]. The zonal-
163 mean zonal wind is relaxed to a time-varying state defined by the daily zonal-mean MERRA zonal
164 wind at a rate of $.05 \text{ d}^{-1}$ to ensure realistic QBO shear throughout the simulation. The vertical
165 grid consists of 130 sigma levels with a uniform resolution of 500 m between the surface and 65
166 km. The top ~ 30 km of the model serves as a sponge layer where wind perturbations are strongly
167 damped with Rayleigh friction. The friction starts from zero at 30 km and ramps up with a tanh
168 function shape to a maximum of 7 d^{-1} above 45 km. An eighth-order horizontal hyper-diffusion
169 is used to prevent energy from accumulating at the smallest model scales. It is set to damp the
170 smallest scale at a rate of 1 d^{-1} . The horizontal resolution is truncated at T120, resulting in a

171 resolution of $\sim 150\text{km}$, a scale chosen to permit simulation of gravity waves resolved in limb-
172 sounding satellite observations [Alexander 2015] that we will use to validate the modeled gravity
173 waves. We force the model with the zonally-symmetric component of the heating removed, and
174 focus on analysis of waves with periods shorter than 30 days.

175 Note that while the horizontal resolution is similar to many current climate models, the spec-
176 tral dynamical core permits resolution of much smaller-scale waves than a typical climate model
177 [Yao and Jablonowski 2015; Holt et al. 2016]. The use of observed rain and cloud properties to
178 force wave in the model provides another advantage over typical climate models which rely of
179 convective parameterization and the ensuing problems [Kiladis et al. 2009; Kim and Alexander
180 2013]. Thirdly, the model’s comparatively high vertical resolution is a key advantage for resolving
181 tropical waves [Holton et al. 2001; Kawatani et al. 2010; Holt et al. 2016].

182 *c. Experiments*

183 We simulate two December periods in 2006 and 2007. These represent, respectively, weak El
184 Niño and moderate La Niña events as seen in the time series of the ENSO 3.4 index shown in
185 Figure 2. Following the characteristic pattern for such conditions, precipitation in the December
186 2006 period was strongest in the central and eastern Pacific, while the precipitation maximum
187 shifted to the Indian Ocean/Maritime Continent region in December 2007. Both Decembers also
188 included significant precipitation variability associated with the Madden-Julian Oscillation (MJO),
189 also shown in Fig. 2. The MJO is only active during the last 13 days of December 2006, while it
190 is active throughout December 2007. For 2006, the MJO activity is focused in the eastern Indian
191 Ocean and Maritime Continent (phases 3-4), whereas in 2007 the signal propagates from Africa
192 to the Maritime Continent (phases 1-4).

193 The properties of waves forced by convective heating are sensitive to both the strength of the
194 heating and the depth of the heating (e.g. Salby and Garcia [1987]; Bergman and Salby [1994];
195 Holton et al. [2002]; Beres [2004]). Geller et al. [2016] suggest that changes in these parameters
196 with ENSO may explain previously observed sensitivity of the QBO to ENSO conditions. Thus
197 to help place our wave analysis results presented later in context, we compare here occurrence
198 frequency distributions of rain rate and cloud-top height for our two cases.

199 Figure 3 compares distributions of tropical rain rates and cloud top heights for December 2006
200 and December 2007 at latitudes most relevant to the QBO (10°S - 10°N). These distributions repre-
201 sent “convective” pixels only, defined as those with rain rates greater than 1.6 mm hr^{-1} . The two
202 distributions are very similar, with no significant differences in the mean values. The La Niña case
203 (2007) displays more of the deepest clouds $>13 \text{ km}$, which is qualitatively consistent with Geller
204 et al. [2016]. The El Niño case (2006) has a few more occurrences of the highest rain rates but
205 also more occurrences of weak rain. There are different fractions of convective pixels overall, only
206 3.5% in December 2007 compared to 4.3% in December 2006. While ENSO dramatically affects
207 the geographical patterns in precipitation, Fig. 3 suggests that globally these statistics of tropical
208 convective rain rate and cloud depth are fairly similar in these two months.

209 4. Results

210 *a. Monthly-mean Patterns in Latent Heating and Tropopause Wind and Temperature*

211 Characteristic patterns associated with El Niño (2006) and La Niña (2007) are clearly visible in
212 the December mean latent heating rates at 400 hPa (Figure 4). Note that rates in Fig. 4 are shown at
213 finer horizontal resolution than the model. To force the model, 30-min heating rates are spectrally

214 decomposed with spatial spherical harmonics and truncated to T120 ($\sim 1.5^\circ$ resolution), and the
215 30-min rates are linearly interpolated in time to the model 3-min timestep.

216 Figure 5 compares December-mean tropopause (~ 17 km) temperature maps for the MERRA
217 reanalysis (left column) and the model (right column). The deepest latent heating in the model
218 extends only to the 15-km level, so these maps represent the dynamical responses to latent heat-
219 ing above those levels that are directly forced. Note that the model initial conditions are zonally
220 symmetric, so all longitudinal variations in temperature result solely from wave responses to the
221 tropospheric heating. The top row shows December 2006 and the bottom row December 2007.
222 The analogous comparison of reanalyses and model monthly-mean zonal winds is shown in Fig-
223 ure 6. In these model monthly-means, we are primarily seeing the projections of the slowly varying
224 equatorial Rossby and Kelvin wave modes on the tropopause temperature and wind structure. The
225 stronger asymmetry in rain and heating across the equator in the 2006 El Niño period leads to
226 stronger responses in the equatorial Rossby waves and characteristic off-equator temperature min-
227 ima. Conversely in 2007, the western Pacific temperature minimum and zonal winds are stronger
228 on the equator and likely also related to the stronger MJO activity there and stronger Kelvin wave
229 responses. Similar tropopause responses to latent heating variations were reported in the idealized
230 model study of Norton [2006].

231 While the model shows differences from MERRA in these monthly-mean comparisons, the de-
232 gree to which our highly idealized model does capture the observed zonally-asymmetric wind and
233 temperature pattern differences in these two years is due to the realism of the monthly-mean heat-
234 ing distribution that is forcing the model. The comparison highlights the importance of waves
235 forced by tropical latent heating in controlling the upper-level circulation and temperature struc-
236 ture.

237 *b. Gravity Wave Spectrum*

238 With heating varying on a 30-min timescale, the response in the model includes a broad spec-
239 trum of gravity waves. We seek to identify relationships between the gravity waves generated
240 by the different latent heating variations, as well as their effects on the circulation in the lower
241 stratosphere. The differences in the zonal mean winds in December 2006 and December 2007
242 are strong at QBO altitudes, beginning at 18 km and above (Fig. 2c). The QBO wind variations
243 will dramatically alter the spectrum of waves through wave-mean flow interaction. We therefore
244 begin here by examining the vertical flux of horizontal momentum, which describes the gravity
245 wave contribution to the EP-flux [Andrews et al. 1987], and we examine this at the tropopause
246 (~ 17 km), which is above the direct latent heating forcing but below the QBO wind influences on
247 the spectrum. This permits an examination of the influences of the tropospheric latent heating and
248 circulation on the vertically propagating wave spectrum in isolation from stratospheric wave-mean
249 flow interactions.

We perform 3-dimensional spectral analysis as a function of longitude, latitude, and time on overlapping 50° longitudinal sectors spanning latitudes $\pm 25^\circ$ over 3-day periods. Wind anomalies in the zonal and meridional directions (u' , v') are computed as deviations from the $50^\circ \times 50^\circ$ sector trends, and cosine taper functions in latitude and longitude are applied. The longitude sectors overlap by 5° on each side where the taper=1/2 such that the total flux in all sector spectra equals the global total, and each spectrum after tapering represents a $\sim 40^\circ \times 40^\circ$ region. The effective horizontal wavelength range resolved in the spectrum is 227-4447 km. Complex 3-dimensional transforms (\hat{U} , \hat{V}) are then multiplied by the complex conjugate of the vertical wind transform \hat{W}^* computed on the same grid, and the real part multiplied by atmospheric density gives the spectral

density of vertical flux of horizontal momentum

$$F_M = \rho [\text{Re}(\hat{U}\hat{W}^*), \text{Re}(\hat{V}\hat{W}^*)] / \Delta k_x / \Delta k_y / \Delta \omega,$$

where (k_x, k_y) is the horizontal wavenumber vector and ω the frequency. The results are rebinned in terms of azimuthal direction of propagation ($^\circ$ from east) and phase speed (c) and renormalized to spectral density in these coordinates. Results for Dec 2006 and 2007 are shown in Figure 7, where we have further reduced the maximum wavelength included in these spectra to wavenumbers > 12 (3335 km). The spectra have been averaged over 15-17 km (above the direct latent heating forcing and below the QBO) to best represent the gravity waves entering the stratosphere prior to their interaction with the QBO winds.

The spectra show some clear differences, but mainly similarities. 2006 shows a weak preference for westward propagation compared to eastward, while 2007 shows a strong peak in the east-northeast direction and relatively weak westward flux. At higher phase speeds, $c > 20 \text{ m s}^{-1}$ the 2006 and 2007 spectra are very similar, displaying a broader westward spectrum and than eastward spectrum. Figure 8 shows the phase speed spectrum of the zonal flux only to highlight waves relevant to the QBO. The La Niña case (2007) has 11% larger zonal flux overall, while the El Niño case shows slightly larger fluxes over a narrow range near $c = -20 \text{ m s}^{-1}$. Meridional fluxes are more similar in the two years. We do not examine asymmetries in gravity waves north and south of the equator, but these have shown sensitivity to ENSO in previous work [Sato et al. 2016].

Figures 9 and 10 examine regional variations in the spectrum. Not surprisingly, these are substantial, and the fluxes vary to some degree with regional variations in the heating. Clearly the ENSO variations in heating give rise to strong regional variations in the gravity wave spectra although the zonal mean spectra (Figs. 7 and 8) were relatively similar. Surprisingly, the strong El

271 Niño heating in the Dec 2006 central Pacific does not result in much stronger gravity wave mo-
 272 mentum fluxes. The reason is likely related to different tropopause winds (Fig. 9c): Tsuchiya et al.
 273 [2016] found stronger tropical gravity wave activity correlated with westward tropopause winds,
 274 while in the central and eastern Pacific those winds are eastward. Note that the spectra over the
 275 Indian Ocean and S. America show secondary peaks in westward propagating waves at the slowest
 276 phase speeds. This is a spectral signature of the obstacle effect for wave generation associated with
 277 the upper troposphere westward winds interacting with deep convection [Alexander et al. 2006].
 278 If these waves were instead generated in the middle troposphere, they would have been filtered by
 279 the upper troposphere westward winds. These regional spectra also make it clear that the strongest
 280 east/west asymmetries occur over these regions plus the African and S. American tropics, where
 281 we see much faster westward phase speeds and much stronger eastward fluxes at $c < 10 \text{ m s}^{-1}$.

282 Figs. 9c and 10c summarize the geographical and interannual variations in tropopause gravity
 283 wave momentum flux more quantitatively. Each symbol represents absolute momentum flux in a
 284 $40^\circ \times 40^\circ$ region, $\pm 20^\circ$ latitude straddling the equator. In both of our simulated years, the Indian
 285 Ocean and Maritime Continent regions are the locus of strongest tropopause gravity waves, where
 286 tropopause winds are also westward. The strongest fluxes in our simulations occur in December
 287 2007 in the sector surrounding Sumatra, a locus of MJO activity throughout an extended portion
 288 of the month (Fig. 2), suggesting that MJO precipitation variability might have greater effect on
 289 gravity wave momentum fluxes than ENSO variability. Note that while a strong peak in total omni-
 290 directional flux occurs in the central Pacific in the 2006 El Niño year, the peak in total zonal flux is
 291 muted due to strong filtering of eastward propagating waves in this region of eastward tropopause
 292 winds. In the 2007 La Niña year we see a peak in the Sumatra sector in total omni-directional
 293 flux as well as a strong peak in zonal flux, which is associated with the peak in eastward waves
 294 (Fig. 9b) propagating through westward tropopause winds.

295 *c. Validation of modeled momentum fluxes*

296 Recent research has highlighted the high degree of intermittency in the occurrence of gravity
297 waves with different amplitudes [Hertzog et al. 2008; 2012; Jewtoukoff et al. 2013; Plougonven
298 et al. 2013; Alexander and Grimsdell 2013; Alexander 2015; Wright et al. 2013]. Observations
299 display log-normal distributions of gravity wave momentum fluxes with infrequent but large events
300 that contain much of the total flux. This high degree of intermittency can be quite important to
301 gravity wave effects on circulation [de la Cámara et al. 2014; Bushell et al. 2015]. Specifically,
302 the larger amplitude waves in the tails of the distributions can break at lower altitudes and result
303 in larger forcing in the stratosphere. Here we examine mean gravity wave momentum fluxes as
304 well as momentum flux occurrence frequency distributions in the model, and we compare both to
305 observations.

306 Zonal and meridional wind anomalies are computed as in section 4.2 and the products of hor-
307 izontal and vertical anomalies and density $\frac{1}{2}\rho((u'w')^2 + (v'w')^2)^{1/2}$ give an estimate of the local
308 momentum flux magnitudes. This method gives accurate maximum values if waves are intermit-
309 tent such that packets appear in relative isolation, an assumption relevant to the lower stratosphere.
310 Ideally, the wind covariances would be averaged over a period or wavelength, however we use this
311 approximate method following previous work [Plougonven et al. 2013].

312 Figure 11a shows occurrence frequencies of these gravity wave momentum fluxes at 20 km, con-
313 trasting Dec 2006 (red) and 2007 (blue), and observations from limb-sounding satellites [Alexan-
314 der 2015] (“HIRDLS/COSMIC”, black). The number of measurements in the satellite retrievals
315 in a single month is too small to fill a distribution, so we use 13 month totals Dec 2006-Dec 2007
316 for comparison to the model results in Fig. 11a. Means of the distributions are 5.2 mPa for the Dec
317 2006 model, and 5.8 mPa for the Dec 2007 model. Averaging the available observations we obtain

318 a mean of 3.2 mPa in Dec 2006 (522 measurements) and 3.9 mPa in Dec 2007 (323 measure-
319 ments). Note that to determine momentum flux from the observations required a wavelet analysis
320 of the vertical structure, so it is not truly a measurement at a single level, but it combines wave
321 amplitude information over a range of altitudes that varies with the wave vertical wavelength. Dec
322 2007 fluxes are larger than Dec 2006 in both the observations and the model.

323 Pre-Concordiasi long-duration balloon measurements covered all longitudes at an altitude near
324 20 km [Jewtoukoff et al. 2013]. The Pre-Concordiasi campaign occurred during a 3 month period
325 February-May, 2010, and the campaign average momentum fluxes from the two tropical balloons
326 were reported at 3.9 and 5.4 mPa. The Pre-Concordiasi values include the spectrum of gravity
327 waves from the buoyancy period to 1-day period, while our model cannot represent waves with
328 periods shorter than 1 hour due to the 30-min resolution of the forcing but includes periods up to 3
329 days. Thus neither the satellite nor the balloon observational comparisons can be considered exact,
330 but these comparisons do suggest the modeled fluxes are reasonably similar to the observations.

331 All of these momentum flux distributions approximately represent log-normal, non-Gaussian
332 distributions. The standard deviation is therefore large compared to the mean value, but this does
333 not indicate a lack of significance. Jewtoukoff et al. [2013] considered the difference between the
334 two Pre-Concordiasi balloons as significant and attributed the difference to geographic sampling:
335 The second balloon with larger mean flux spent more time above the Indian Ocean/West Pacific
336 Ocean sectors where the occurrence of multicellular convection was concentrated and where we
337 also see largest momentum fluxes. Similarly, it is likely that the differences between the model
338 in Dec 2006 and Dec 2007 are also significant given the distinct peaks in the fluxes seen in the
339 spectrum (Fig. 7). However, the uncertainties in the heating derived from CMORPH precipitation
340 would also need to be considered in order to claim a statistically significant difference between

the two cases. Both the 3D satellite observations and the model suggest somewhat larger fluxes in Dec 2007 than in Dec 2006.

At 20 km, QBO wind shears will have filtered some of the gravity waves. To isolate differences associated with the tropical tropospheric conditions in the two years, we also show modeled momentum flux distributions at the tropopause (~ 17 km) in Fig. 11b, an altitude just below the QBO shear zones. Note the expanded abscissa range to show the higher values that occur at this altitude. Here interannual differences appear more prominently in the extended tail of the distribution, and statistics for these distributions are shown in Table 1. The percentile statistics indicate that in Dec 2007 for example, fluxes larger than 20 mPa occur only 10% of the time (90th percentile) but correspond to 54% of the total flux. This indicates that while convective waves are not quite as intermittent as orographic waves observed over Southern Hemisphere topography [Hertzog et al. 2012; de la Cámara and Lott 2015], the convective waves display a substantially larger degree of intermittency than is commonly assumed in non-orographic gravity wave parameterizations (see Bushell et al. [2015]). By comparing our mean tropopause fluxes to the 20 km values given earlier, a large fraction ($\sim 45\%$) of the flux has already dissipated in QBO shear zones below 20 km.

d. QBO Wave Driving

We can also examine the tropical wave EP-fluxes and flux divergences in the model. EP-flux divergence is a measure of the model-resolved wave drag forces acting on the QBO. We also investigate the types of waves responsible for these forces in the model.

Figure 12 shows zonal wavenumber-frequency spectra of the absolute value of the vertical component of the EP-flux at 20 km and profiles of the divergence of this flux in Dec 2006 (a,b) and 2007 (c,d). In b and d, two profiles of each color represent separate integrations over eastward-only (positive) or westward-only (negative) wavenumbers. Black profiles represent integrals over

the full halves of the spectrum. Red profiles are integrals over only the planetary-scale waves, which we define as frequencies less than 1 cyc d^{-1} and wavenumbers less than 12, illustrated with a small box near the origin in the two figures. The differences between red and black profiles then show the contributions from eastward and westward propagating gravity waves to the force on the circulation.

In 2006, gravity waves account for almost all the westward forcing, whereas in 2007 the eastward forcing is more equally proportioned between gravity waves and Kelvin waves. Note also that in both cases contributions from gravity waves are substantial even below 20km. Close examination of the two panels in Fig. 11 reveal that changes in the momentum flux distributions between 17 km and 20 km are mostly due to the loss of infrequently occurring, large amplitude waves, and similar changes with altitude have also been seen in other models [Hertzog et al. 2012]. We note that these large amplitude waves are missing in parameterizations of convective gravity wave drag (see Bushell et al. [2015]), which may explain why models tend to poorly represent the QBO in the lower stratosphere. Conversely, our model with realistic distributions in gravity wave sources (i.e. latent heating) generates a much more realistic distribution of gravity wave amplitudes, and hence significant gravity wave forces in the lowermost stratosphere.

5. Discussion

Recent work has shown clearly the very intermittent nature of gravity waves. The intermittency in our simulations (Fig. 11a) compares well to observations at an altitude near 20 km. Bushell et al. [2015] show tropical momentum flux distributions for different gravity wave parameterizations (their Fig. 6). Their invariant non-orographic parameterization dropped 4 decades in occurrence at a flux of 6 mPa. Essentially, all of the waves in the parameterization are weak in amplitude and not intermittent. They also showed the distribution of gravity wave momentum fluxes using a

387 variable convective source parameterization. In this case, occurrences drop 4 decades at a flux of
388 $\sim 20\text{-}25$ mPa, which is much more realistically intermittent than the invariant parameterization, but
389 the intermittency falls far short of that observed or that produced in our model. In particular, long-
390 duration balloon observations [Jewtoukoff et al. 2013] (their Fig. 15) show that the momentum
391 fluxes drop 4 decades in occurrence at flux values ~ 100 mPa, and this occurs at ~ 80 mPa in
392 our simulations. There is evidence that incorporating this more realistic intermittency into gravity
393 wave parameterizations can improve stratospheric circulation in climate models [de la Cámara et
394 al. 2016]

395 Typical invariant non-orographic gravity wave parameterizations have only very weak forces in
396 the stratosphere. They are designed instead to give realistic circulation effects in the mesosphere.
397 Orographic gravity waves are parameterized with much larger amplitudes than non-orographic
398 waves, and as a result they break and change the circulation in the upper troposphere and lower
399 stratosphere. However, large amplitude waves from convection do occur, and the momentum
400 flux convergences in the stratosphere can lead to substantial forces. For example, Stephan et al.
401 [2016] showed that realistic waves from summertime convection over the U.S. produce forces
402 in the lower stratosphere that rival orographic wave forcing. Most parameterizations in models
403 give relatively very small wave forces at stratospheric levels. Stochastic non-orographic parame-
404 terization methods that account for realistically intermittent amplitudes have been developed [de
405 la Cámara and Lott 2015], and implementation in a global model showed improvements in the
406 timing of the springtime transition from westerly to easterly winds in the Southern Hemisphere
407 stratosphere [de la Cámara et al. 2016]. So including realistic intermittency in parameterized
408 non-orographic gravity wave amplitudes, while simultaneously reducing gravity wave drag due
409 to orographic waves, may be a way forward. Indeed, climate models struggle to simultaneously

410 simulate realistic Northern and Southern Hemispheric stratospheric winds, which could be due to
411 an over-reliance on orographic gravity wave drag.

412 Similarly, we find support for much larger intermittency in tropical convective gravity waves
413 than is typically parameterized, and we hypothesize this is the reason that models struggle to
414 represent realistic QBO winds and wind shears in the lower stratosphere at levels below 40 hPa
415 (e.g. Krismer and Giorgetta [2014]; Richter et al. [2014]; Coy et al. [2016]). Typical gravity
416 wave parameterizations drive only the upper levels of the QBO while planetary scale waves are
417 responsible for most or all of the forcing at the lower levels. An early example with an invariant
418 parameterization was shown in Giorgetta et al. [2002]. More recently Richter et al. [2014] showed
419 modern results with a variable convective source parameterization that gave a very realistic QBO
420 at pressure levels above 40 hPa, but in the lower stratosphere the westerly phases are too strong and
421 easterly phases too weak. Yoo and Son [2016] have shown that easterly QBO winds in the lower
422 stratosphere are associated with stronger tropical intraseasonal precipitation in the observational
423 record. Hence such errors in modeled QBO winds may hinder a model's ability to represent the
424 observed stratosphere-troposphere connections. We also note that many previous studies have
425 suggested that the easterly QBO wind phases are forced primarily by gravity wave drag (e.g.
426 Dunkerton [1997]; Kawatani et al. [2010]).

427 More realistic intermittency such as shown in our Fig. 11 does in fact lead to significant forces
428 in the lower stratosphere below 20 km (Fig. 12). That these forces are due to dissipation of the
429 largest amplitude waves is also evident from comparison of the distributions at 17 km and 20 km
430 shown in Fig. 11. Nearly half of the gravity wave momentum flux is dissipated between these
431 levels in our model.

432 Our results may be relevant for realizing the long-range forecast skill that is expected from re-
433 alistic representation of the tropical stratosphere in forecast models. Although the Scaife et al.

[2014a] study found the QBO among the four leading sources of skill in their winter seasonal forecasts of the NAO, their forecast model's QBO teleconnection pattern was weaker than in the observations. As mentioned above, model representations of the QBO tend to be least realistic at low levels below 40 hPa, and discrepancies in the width of the QBO are also common [O'Sullivan and Young 1992; Hansen et al. 2013]: Either or both of these could be reasons for weaker teleconnections in models. Maximum correlations between extratropical winter conditions and QBO winds have been observed with 50 hPa QBO wind in observations. If the lower levels of the QBO are unduly important to describing extratropical teleconnection strength, it points to a clear weakness in models. Further, the results of Yoo and Son [2016] suggest that long-range forecasting skill in tropical intraseasonal precipitation may be tied to realistic representation of the QBO at lower stratosphere levels in models.

While studies have shown the QBO to be highly predictable on time scales longer than a year [Scaife et al. 2014b] the unprecedented disruption of the QBO in 2016 and the failure of forecast models to predict its subsequent evolution at 10 hPa [Newman et al. 2016 (and recorded presentation <https://ams.confex.com/ams/97Annual/webprogram/Paper301482.html>); Osprey et al. 2016] place new emphasis on more realistic representation of the wave forcing of the QBO. There is also observational evidence that the QBO winds at low levels near 70 hPa may be experiencing a long-term weakening trend [Kawatani and Hamilton 2013]. Hence more realistic simulation of the QBO may also be beneficial to near-term climate prediction as well as seasonal forecast model skill.

In addition to forcing the stratosphere and mesosphere, gravity waves from convection can also directly force the circulation in the upper atmosphere and ionosphere [Vadas and Liu 2013; Vadas et al. 2014]. The gravity waves that can propagate to these high altitudes have fast phase speeds, faster than $\sim 50 \text{ m s}^{-1}$. While the peaks in our integrated phase spectra (Figs. 7-8) occurred at

458 phase speeds $\sim 7\text{--}20 \text{ m s}^{-1}$, the spectra in Fig. 12 show that much faster waves also appear at
 459 higher frequencies. In particular, a lobe with phase speeds of 70 m s^{-1} among the westward prop-
 460 agating highest frequencies is prominent. According to the linear dispersion relation (neglecting
 461 wind effects) vertical wavelength $\lambda_z \sim 2\pi c/N$, these fast waves would have $\lambda_z \sim 44 \text{ km}$ in the
 462 troposphere, which is close to four times the most common cloud and heating depth in our simula-
 463 tions of 11 km (Fig. 3). While a vertical wavelength of twice the depth of the heating, or 22 km , is
 464 predicted for large-scale heat sources, Holton et al. [2002] showed that smaller-scale heat sources
 465 will project more strongly on vertical wavelengths four times the depth of the heating. Our model
 466 simulations support the Holton et al. [2002] result, and show that such fast waves clearly appear
 467 in our simulations. In fact, they can dominate the convectively-generated gravity wave spectrum
 468 at wave periods shorter than a few hours.

469 **6. Summary and Conclusions**

470 We use satellite-based global precipitation and cloud data at high spatial and temporal reso-
 471 lution to estimate three-dimensional time-varying latent heating and the resulting global wave
 472 spectrum generated. The modeled zonally-averaged gravity wave momentum fluxes in the lower
 473 stratosphere are similar to those derived from 3D satellite data, and similar to those observed by
 474 Pre-Concordiasi long-duration balloons. Modeled distributions of gravity wave momentum fluxes
 475 also display similar intermittency to the Pre-Concordiasi balloon measurements. These compar-
 476 isons show that the modeled zonally-averaged fluxes fall within the range of variability seen in
 477 observations.

478 Interannual variations in gravity waves were examined in the context of interannual precipitation
 479 variations in Decembers of 2006 and 2007. Spectra and intermittency of momentum flux were
 480 also evaluated. Profiles of momentum flux convergence were used to examine gravity wave forces

481 acting on the QBO shear zones, and these forces were compared to planetary-scale tropical wave
482 forces. The results show that in the zonal mean sense, the changes with ENSO are only modest,
483 although regional variations in the gravity waves are large. For example, despite more rain and
484 latent heating in the El Niño case, the zonal gravity wave momentum fluxes are 11% smaller at the
485 tropopause than in the La Niña case because of the shift in the precipitation to the central Pacific
486 where upper tropospheric zonal winds are less favorable for vertical wave propagation. The more
487 active MJO convection in the Indian Ocean/Maritime Continent region in the La Niña case appears
488 to be a more important source in terms of gravity wave momentum fluxes.

489 The modeled intermittency in gravity wave amplitudes is similar to that observed in existing
490 drifting isopycnal balloon measurements [Jewtoukoff et al. 2013], but current parameterization
491 methods significantly underestimate this degree of intermittency in gravity waves above tropical
492 convection, even with more realistic convective source parameterizations. Stochastic parameteri-
493 zation methods such as described in de la Cámara and Lott [2015] could be applied to the tropics
494 utilizing these intermittency statistics, and we show evidence to suggest that such intermittency
495 could improve the simulation of the QBO at lower levels where models show clear weaknesses,
496 below ~ 22 km (40 hPa). We further hypothesize that improving the simulation of the QBO at these
497 lower altitudes might improve simulation of tropical-extratropical teleconnections and associated
498 skill in long-range weather and seasonal climate forecasts.

499 In the future, we may have better observations to validate the inter-annual and regional variations
500 in gravity wave momentum flux predicted in our model. Future measurements planned during the
501 STRATEOLE-2 field campaign (www.strateole2.org) will provide a wealth of observations for
502 model validation. Beginning in 2014, new precipitation measurements in the Global Precipitation
503 Measurement (GPM) era have led to a new 30-min, $0.1^\circ \times 0.1^\circ$ resolution IMERG rain rate product
504 [Huffmann et al., 2015]. These data are reportedly better constrained at higher frequencies, and

505 may provide more accurate forcing for future model studies that can be more thoroughly validated
506 with observations from STRATEOLE-2.

507 *Acknowledgments.* This work was supported by National Aeronautics and Space Administra-
508 tion’s Aura Science Team program, with grants NNX14AE82G and NNX17AF55G.

509 APPENDIX

510 **Latent Heating**

511 The latent heating algorithm we use to compute space-time gridded heating rates suitable for
512 wave studies was described in Ryu et al. [2011]. There, they showed the zonal-mean heating
513 profiles as functions of latitude in comparison to version 1 of the TRMM CSH latent heating
514 product. Changes in version 2 of CSH resulted in stronger rates and a shift downward in the
515 altitude of the peak heating. (See Tao et al. [2010]: their Fig. 10.) Considering these changes,
516 our heating algorithm compared reasonably well in the mean to CSH. No high-frequency latent
517 heating products exist for us to compare the higher-frequency variability. We instead validate our
518 modeled gravity waves with observations in section 4.

519 A further examination of the heating input to the model is shown in Figure A1. These are average
520 heating profiles over land and ocean regions within $\pm 30^\circ$ latitude for Dec 2006 and Dec 2007. The
521 heating profile shapes compare well to the TRMM SLH 15-yr means over land shown in Liu et
522 al. [2015], although these ocean profiles display weaker secondary shallow heating than the 15-yr
523 SLH means. The El Niño year (Dec 2006) shows less difference between heating over land and
524 ocean than the La Niña year (Dec 2007), which is not surprising given the shifts in precipitation
525 evident from Fig. 4. The active MJO during both of these months may be responsible for the

526 higher peak heating magnitudes in these cases compared to multi-year means [Tao et al. 2010; Liu
527 et al. 2015].

528 **References**

529 Alexander, M. J., 2015: Global and seasonal variations in three-dimensional gravity wave momen-
530 tum flux from satellite limb-sounding temperatures. *Geophys. Res. Lett.*, **42** (16), 6860–6867,
531 doi:10.1002/2015GL065234.

532 Alexander, M. J., and A. W. Grimsdell, 2013: Seasonal cycle of orographic gravity wave occur-
533 rence above small islands in the Southern Hemisphere: Implications for effects on the general
534 circulation. *J. Geophys. Res.: Atmos.*, **118** (20), 11,589–11,599, doi:10.1002/2013JD020526.

535 Alexander, M. J., J. H. Richter, and B. R. Sutherland, 2006: Generation and trapping of gravity
536 waves from convection, with comparison to parameterization. *J. Atmos. Sci.*, **63** (11), 2963–
537 2977.

538 Andrews, D. G., J. R. Holton, and C. B. Leovy, 1987: *Middle Atmosphere Dynamics*. Academic
539 Press, Orlando, 489 pp. pp.

540 Anstey, J. A., and T. G. Shepherd, 2014: High-latitude influence of the quasi-biennial oscillation.
541 *Quar. J. Roy. Meteorol. Soc.*, **140** (678), 1–21, doi:10.1002/qj.2132.

542 Beres, J., 2004: Gravity wave generation by a 3-dimensional thermal forcing. *J. Atmos. Sci.*, **61**,
543 1805–1815.

544 Bergman, J. W., and M. L. Salby, 1994: Equatorial wave activity derived from fluctuations in
545 observed convection. *J. Atmos. Sci.*, **51**, 3791–3806.

546 Bushell, A. C., N. Butchart, S. H. Derbyshire, D. R. Jackson, G. J. Shutts, S. B. Vosper, and
 547 S. Webster, 2015: Parameterized gravity wave momentum fluxes from sources related to con-
 548 vection and large-scale precipitation processes in a global atmosphere model. *J. Atmos. Sci.*,
 549 **72** (11), 4349–4371, doi:10.1175/JAS-D-15-0022.1.

550 Coy, L., K. Wargan, A. M. Molod, W. R. McCarty, and S. Pawson, 2016: Structure and
 551 dynamics of the quasi-biennial oscillation in MERRA-2. *J. Climate*, **29**, null, doi:10.1175/
 552 JCLI-D-15-0809.1.

553 de la Cámara, A., and F. Lott, 2015: A parameterization of gravity waves emitted by fronts and
 554 jets. *Geophys. Res. Lett.*, **42** (6), 2071–2078, doi:10.1002/2015GL063298.

555 de la Cámara, A., F. Lott, V. Jewtoukoff, R. Plougonven, and A. Hertzog, 2016: On the gravity
 556 wave forcing during the southern stratospheric final warming in LMDz. *J. Atmos. Sci.*, **73** (8),
 557 3213–3226, doi:10.1175/JAS-D-15-0377.1.

558 dela Cámara, A., F. Lott, and A. Hertzog, 2014: Intermittency in a stochastic parameterization of
 559 nonorographic gravity waves. *J. Geophys. Res. Atmos.*, **119** (21), 11,905–11,919, doi:10.1002/
 560 2014JD022002.

561 Dunkerton, T., 1997: The role of gravity waves in the quasi-biennial oscillation. *J. Geophys. Res.*,
 562 **102**, 26,053–26,076.

563 Garfinkel, C. I., T. A. Shaw, D. L. Hartmann, and D. W. Waugh, 2012: Does the Holton-Tan
 564 mechanism explain how the quasi-biennial oscillation modulates the Arctic polar vortex? *J.*
 565 *Atmos. Sci.*, **69** (5), 1713–1733.

566 Geller, M. A., T. Zhou, and W. Yuan, 2016: The QBO, gravity waves forced by tropical convection,
 567 and ENSO. *J. Geophys. Res. Atmos.*, **121** (15), 8886–8895, doi:10.1002/2015JD024125.

568 Geller, M. A., and Coauthors, 2013: A comparison between gravity wave momentum fluxes in
 569 observations and climate models. *J. Climate*, **26**, 6383–6405.

570 Giorgetta, M. A., E. Manzini, and E. Roeckner, 2002: Forcing of the quasi-biennial oscillation
 571 from a broad spectrum of atmospheric waves. *Geophys. Res. Lett.*, **29** (8), 86–1 to 86–4.

572 Habib, E., A. T. Haile, Y. Tian, and R. J. Joyce, 2012: Evaluation of the high-resolution CMORPH
 573 satellite rainfall product using dense rain gauge observations and radar-based estimates. *J. Hy-*
 574 *drometeorol.*, **13** (6), 1784–1798, doi:10.1175/JHM-D-12-017.1.

575 Hansen, F., K. Matthes, and L. J. Gray, 2013: Sensitivity of stratospheric dynamics and chem-
 576 istry to QBO nudging width in the chemistry-climate model WACCM. *Journal of Geophysical*
 577 *Research: Atmospheres*, **118** (18), 10,464–10,474, doi:10.1002/jgrd.50812.

578 Held, I. M., and M. J. Suarez, 1994: A proposal for the intercomparison of the dynamical cores
 579 of atmospheric general circulation models. *Bull. Am. Meteorol. Soc.*, **75** (10), 1825–1830, doi:
 580 10.1175/1520-0477(1994)075<1825:APFTIO>2.0.CO;2.

581 Hertzog, A., M. J. Alexander, and R. Plougonven, 2012: On the intermittency of gravity-wave
 582 momentum flux in the stratosphere. *J. Atmos. Sci.*, **69**, 3433–3448.

583 Hertzog, A., G. Boccara, R. A. Vincent, F. Vial, and P. Cocquerez, 2008: Estimation of
 584 gravity wave momentum flux and phase speeds from quasi-Lagrangian stratospheric balloon
 585 flights. Part II: Results from the VORCORE campaign in Antarctica. *J. Atmos. Sci.*, **65** (DOI:
 586 **10.1175/2008JAS2710.1**), 3056–3070.

587 Holt, L. A., M. J. Alexander, L. Coy, A. Molod, W. Putman, and S. Pawson, 2016: Tropical
 588 waves and the quasi-biennial oscillatioin in a 7-km global climate simulation. *J. Atmos. Sci.*, **73**,
 589 3771–3783.

590 Holton, J., J. Beres, and X. Zhou, 2002: On the vertical scale of gravity waves excited by localized
 591 thermal forcing. *J. Atmos. Sci.*, **59**, 2019–2023.

592 Holton, J. R., M. J. Alexander, and M. T. Boehm, 2001: Evidence for short vertical wavelength
 593 Kelvin waves in the Department of Energy-Atmospheric Radiation Measurement Nauru99 ra-
 594 diosonde data. *J. Geophys. Res.*, **106**, 20,125–20,129.

595 Holton, J., and H.-C. Tan, 1980: The influence of the equatorial quasi-biennial oscillation on the
 596 global circulation at 50 mb. *J. Atmos. Sci.*, **37**, 2200–2208.

597 Holton, J. R., and W. M. Wehrbein, 1980: The role of forced planetary waves in the annual cycle
 598 of the zonal mean circulation of the middle atmosphere. *J. Atmos. Sci.*, **37** (9), 1968–1983,
 599 doi:10.1175/1520-0469(1980)037<1968:TROFPW>2.0.CO;2.

600 Huffman, G., D. T. Bolvin, D. Braithwaite, K. Hsu, R. Joyce, and P. Xie, 2015: NASA global
 601 precipitation measurement (GPM) integrated multi-satellite retrievals for GPM (IMERG). *Al-*
 602 *gorithm Theoretical Basis Document (ATBD)*, Version 4.5, NASA/GSFC, 30 pp.

603 Huffman, G. J., and Coauthors, 2007: The TRMM Multisatellite Precipitation Analysis (TMPA):
 604 Quasi-global, multiyear, combined-sensor precipitation estimates at fine scales. *J. Meteorol.*, **8**,
 605 38–55.

606 Jewtoukoff, V., R. Plougonven, and A. Hertzog, 2013: Gravity waves generated by deep tropical
 607 convection: Estimates from balloon observations and mesoscale simulations. *J. Geophys. Res.*
 608 *Atmos.*, **118** (17), 9690–9707, doi:10.1002/jgrd.50781.

609 Joyce, R. J., J. E. Janowiak, P. A. Arkin, and P. Xie, 2004: CMORPH: A method that produces
 610 global precipitation estimates from passive microwave and infrared data at high spatial and

temporal resolution. *J. Hydrometeorol.*, **5**, 487–503. [Data available online at http://www.cpc.ncep.noaa.gov/products/janowiak/cmorph_description.html]

Kawatani, Y., and K. Hamilton, 2013: Weakened stratospheric quasibiennial oscillation driven by increased tropical mean upwelling. *Nature*, **497**, 478–481.

Kawatani, Y., K. Sato, T. J. Dunkerton, S. Watanabe, S. Miyahara, and M. Takahashi, 2010: The roles of equatorial trapped waves and three-dimensionally propagating gravity waves in driving the quasi-biennial oscillation. Part I: Zonal mean wave forcing. *J. Atmos. Sci.*, **67**, 963–980.

Kiladis, G. N., M. C. Wheeler, P. T. Haertel, K. H. Straub, and P. E. Roundy, 2009: Convectively coupled equatorial waves. *Rev. Geophys.*, **47**, 1–42.

Kim, J.-E., and M. J. Alexander, 2013: Tropical precipitation variability and convectively coupled equatorial waves on submonthly time scales in reanalyses and TRMM. *J. Climate*, **26**, 3013–3030.

Krismer, T. R., and M. A. Giorgetta, 2014: Wave forcing of the quasi-biennial oscillation in the Max Planck Institute Earth System Model. *J. Atmos. Sci.*, **71** (6), 1985–2006.

Liu, C., S. Shige, Y. N. Takayabu, and E. Zipser, 2015: Latent heating contribution from precipitation systems with different sizes, depths, and intensities in the tropics. *J. Climate*, **28** (1), 186–203.

Mote, P., and Coauthors, 1996: An atmospheric tape recorder: The imprint of tropical tropopause temperatures on stratospheric water vapor. *J. Geophys. Res.*, **101**, 3989–4006.

Newman, P. A., L. Coy, S. Pawson, and L. R. Lait, 2016: The anomalous change in the QBO in 2015/2016. *Geophys. Res. Lett.*, **43** (16), 8791–8797, doi:10.1002/2016GL070373.

632 Norton, W. A., 2006: Tropical wave driving of the annual cycle in tropical tropopause tempera-
633 tures. Part II: Model results. *J. Atmos. Sci.*, **63** (May 2006), 1420–1431.

634 Ortland, D. A., M. J. Alexander, and A. W. Grimsdell, 2011: On the wave spectrum generated by
635 latent heating. *J. Atmos. Sci.*, **68**, 2042–2060.

636 Osprey, S. M., N. Butchart, J. R. Knight, A. A. Scaife, K. Hamilton, J. A. Anstey, V. Schenzinger,
637 and C. Zhang, 2016: An unexpected disruption of the atmospheric quasi-biennial oscillation.
638 *Science*, **353** (6306), 1424–1427, doi:10.1126/science.aah4156.

639 O’Sullivan, D., and R. E. Young, 1992: Modeling the quasi-biennial oscillation’s effect on the win-
640 ter stratospheric circulation. *J. Atmos. Sci.*, **49** (24), 2437–2448, doi:10.1175/1520-0469(1992)
641 049<2437:MTQBOE>2.0.CO;2.

642 Plougonven, R., A. Hertzog, and L. Guez, 2013: Gravity waves over Antarctica and the South-
643 ern Ocean: Consistent momentum fluxes in mesoscale simulations and stratospheric balloon
644 observations. *Q. J. Roy. Meteorol. Soc.*, **139**, 101–118.

645 Randel, W. J., F. Wu, S. J. Oltmans, K. Rosenlof, and G. E. Nedoluha, 2004: Interannual changes
646 of stratospheric water vapor and correlations with tropical tropopause temperatures. *J. Atmos.*
647 *Sci.*, **61**, 2133–2148.

648 Richter, J. H., A. Solomon, and J. T. Bacmeister, 2014: On the simulation of the quasi-biennial
649 oscillation in the Community Atmosphere Model, version 5. *J. Geophys. Res. Atmos.*, **119**,
650 3045–3062, doi:10.1002/2013JD021122.

651 Rienecker, M. M., and et al., 2011: MERRA: NASA’s Modern-Era Retrospective analysis for
652 Research and Applications. *J. Climate*, **24**, 3624–3648. [Available online at [https://gmao.gsfc.
653 nasa.gov/reanalysis/MERRA/](https://gmao.gsfc.nasa.gov/reanalysis/MERRA/)]

654 Ryu, J.-H., M. J. Alexander, and D. A. Ortland, 2011: Equatorial waves in the upper troposphere
655 and lower stratosphere forced by latent heating estimated from TRMM rain rates. *J. Atmos. Sci.*,
656 **68**, 2321–2342.

657 Salby, M. L., and R. Garcia, 1987: Transient response to localized episodic heating in the tropics.
658 Part I: Excitation and short-time near-field behaviour. *J. Atmos. Sci.*, **44**, 458–498.

659 Sapiano, M. R. P., and P. A. Arkin, 2009: An intercomparison and validation of high-resolution
660 satellite precipitation estimates with 3-hourly gauge data. *Journal of Hydrometeorology*, **10** (1),
661 149–166, doi:10.1175/2008JHM1052.1.

662 Sato, K., C. Tsuchiya, M. J. Alexander, and L. Hoffmann, 2016: Climatology and ENSO-related
663 interannual variability of gravity waves in the Southern Hemisphere subtropical stratosphere
664 revealed by high-resolution AIRS observations. *J. Geophys. Res. Atmos.*, **121** (13), 7622–7640,
665 doi:10.1002/2015JD024462.

666 Scaife, A. A., and Coauthors, 2014b: Predictability of the quasi-biennial oscillation and its north-
667 ern winter teleconnection on seasonal to decadal timescales. *Geophys. Res. Lett.*, **41** (5), 1752–
668 1758, doi:10.1002/2013GL059160.

669 Scaife, A. A., and Coauthors, 2014a: Skillful long-range prediction of European and North Amer-
670 ican winters. *Geophysical Research Letters*, **41** (7), 2514–2519, doi:10.1002/2014GL059637,
671 URL <http://dx.doi.org/10.1002/2014GL059637>.

672 Schenzinger, V., and Coauthors, 2016: Defining metrics of the Quasi-Biennial Oscillation in
673 global climate models. *Geophys. Model Dev. Disc.*, **41** (7), 2514–2519, doi:doi:10.5194/
674 gmd-2016-284, URL <http://www.geosci-model-dev-discuss.net/gmd-2016-284/>.

675 Schirber, S., E. Manzini, T. Krismer, and M. Giorgetta, 2015: The quasi-biennial oscillation
676 in a warmer climate: Sensitivity to different gravity wave parameterizations. *Climate Dy-*
677 *namics*, **45** (3-4), 825–836, doi:10.1007/s00382-014-2314-2, URL [http://dx.doi.org/10.1007/](http://dx.doi.org/10.1007/s00382-014-2314-2)
678 [s00382-014-2314-2](http://dx.doi.org/10.1007/s00382-014-2314-2).

679 Shige, S., Y. N. Takayabu, W.-K. Tao, and C.-L. Shie, 2007: Spectral retrieval of latent heat-
680 ing profiles from TRMM PR data. Part 2: Algorithm improvement and heating estimates over
681 tropical ocean regions. *J. Appl. Meteorol. and Clim.*, **46**, 1098–1124.

682 Stephan, C., M. J. Alexander, and J. H. Richter, 2016: Characteristics of gravity waves from
683 convection and implications for their parameterization in global circulation models. *Journal of*
684 *the Atmospheric Sciences*, **73** (7), 2729–2742, doi:10.1175/JAS-D-15-0303.1.

685 Tao, W.-K., S. Lang, X. Zeng, S. Shige, and Y. Takayabu, 2010: Relating convective and stratiform
686 rain to latent heating. *J. Climate*, **23**, 1874–1893.

687 Thompson, D. W. J., M. P. Baldwin, and J. M. Wallace, 2002: Stratospheric connection to Northern
688 Hemisphere wintertime weather: Implications for prediction. *J. Climate*, **15**, 1421–1428.

689 TRMM Ancillary Data, 2016: Globally-merged Full Resolution IR Brightness Temperature Data.
690 [Available online at https://disc.gsfc.nasa.gov/TRMM/data-holdings/data_access.html]

691 Tsuchiya, C., K. Sato, M. J. Alexander, and L. Hoffmann, 2016: MJO-related intraseasonal
692 variation of gravity waves in the Southern Hemisphere tropical stratosphere revealed by high-
693 resolution AIRS observations. *J. Geophys. Res. Atmos.*, **121** (13), 7641–7651, doi:10.1002/
694 2015JD024463.

- 695 Ushio, T., and Coauthors, 2009: A Kalman filter approach to the global satellite mapping of
696 precipitation (GSMAP) from combined passive microwave and infrared radiometric data. *J.*
697 *Meteorol. Soc. Japan*, **87A**, 137–151.
- 698 Vadas, S. L., and H.-L. Liu, 2013: Numerical modeling of the large-scale neutral and plasma
699 responses to the body forces created by the dissipation of gravity waves from 6 h of deep
700 convection in Brazil. *Journal of Geophysical Research: Space Physics*, **118** (5), 2593–2617,
701 doi:10.1002/jgra.50249.
- 702 Vadas, S. L., H.-L. Liu, and R. S. Lieberman, 2014: Numerical modeling of the global changes
703 to the thermosphere and ionosphere from the dissipation of gravity waves from deep con-
704 vection. *Journal of Geophysical Research: Space Physics*, **119** (9), 7762–7793, doi:10.1002/
705 2014JA020280.
- 706 Wheeler, M. C., and H. H. Hendon, 2004: An all-season real-time multivariate MJO index: De-
707 velopment of an index for monitoring and prediction. *Mon. Wea. Rev.*, **132** (8), 1917–1932,
708 doi:10.1175/1520-0493(2004)132<1917:AARMMI>2.0.CO;2.
- 709 Wright, C. J., S. M. Osprey, and J. C. Gille, 2013: Global observations of gravity wave inter-
710 mittency and its impact on the observed momentum flux morphology. *J. Geophys. Res. Atmos.*,
711 **118** (19), 10,980–10,993, doi:10.1002/jgrd.50869.
- 712 Yao, W. and C. Jablonowski, 2015: Idealized quasi-biennial oscillations in an ensemble of dry
713 GCM dynamical cores. *J. Atmos. Sci.*, **72**, 2201–2226.
- 714 Yoo, C., and S.-W. Son, 2016: Modulation of the boreal wintertime Madden-Julian oscillation
715 by the stratospheric quasi-biennial oscillation. *Geophys. Res. Lett.*, **43** (3), 1392–1398, doi:
716 10.1002/2016GL067762.

717	LIST OF TABLES	
718	Table 1. Tropopause Momentum Flux Distribution Statistics	35

TABLE 1. Tropopause Momentum Flux Distribution Statistics

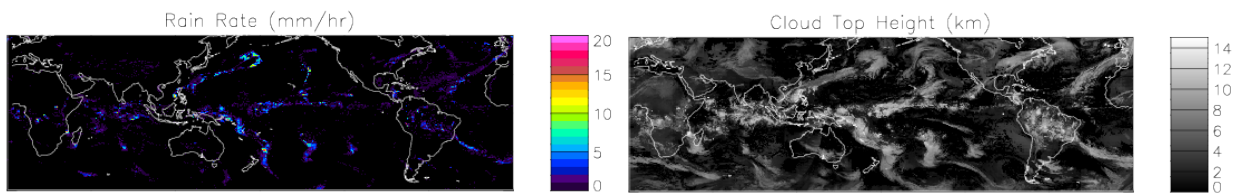
	Mean	90 th	99 th
	(mPa)	Percentile	Percentile
Dec 2006	9.5	19mPa/49%	46mPa/14%
Dec 2007	11	20mPa/54%	51mPa/18%

LIST OF FIGURES

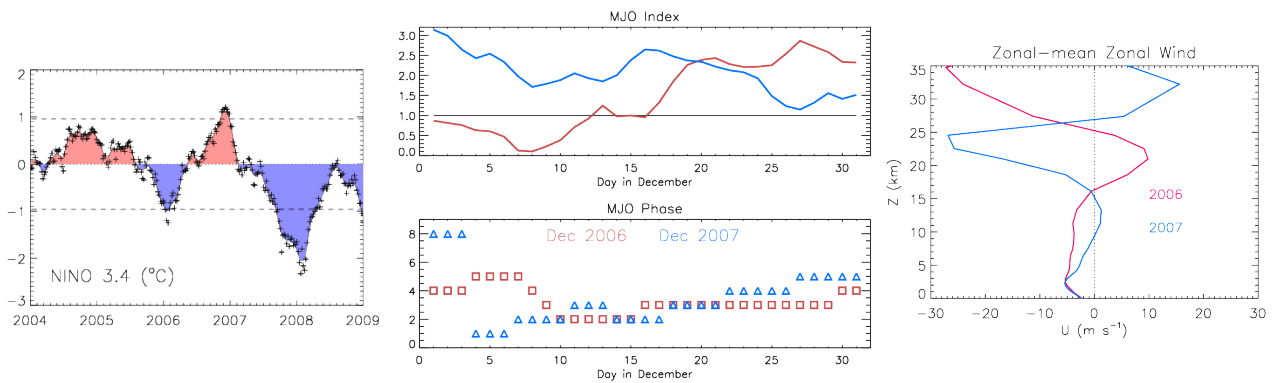
720	Fig. 1.	Example snapshots of $0.25^\circ \times 0.25^\circ$ resolution rain rates (left) and cloud top heights (right)	
721		at 03:00 UT on 1 Dec 2006.	38
722	Fig. 2.	Left: Time series of the monthly ENSO 3.4 sea surface temperature anomaly showing De-	
723		cember 2006 and December 2007 as weak El Niño ($>+1^\circ$) and moderate La Niña ($<-1.5^\circ$)	
724		events, respectively. (Data source: NOAA/ESRL/PSD.) Center: MJO index (top) and phase	
725		(bottom) for Dec 2006 (red) and Dec 2007 (blue) as defined by the MJO Multivariate Index	
726		[Wheeler and Hendon, 2004]. Right: Wind profiles for Dec 2006 (red) and Dec 2007 (blue).	39
727	Fig. 3.	Distributions of tropical 10°S - 10°N rain rates (left) and cloud top heights (right) at $0.25^\circ \times$	
728		0.25° resolution for “convective rain” points, those with rates exceeding 1.6 mm hr^{-1} . Col-	
729		ors indicate Dec 2006 (red) and Dec 2007 (blue).	40
730	Fig. 4.	Monthly-averaged 400 hPa latent heating (K hr^{-1}) mapped 60°S - 60°N for December 2006	
731		(left) and December 2007 (right) shown at $0.25^\circ \times 0.25^\circ$ resolution. The patterns illustrate	
732		typical ENSO variability.	41
733	Fig. 5.	Monthly-mean tropopause temperatures for Dec 2006 (top row) and Dec 2007 (bottom row).	
734		Left: MERRA reanalysis. Right: Model.	42
735	Fig. 6.	Monthly-mean 100hPa zonal winds for Dec 2006 (top row) and Dec 2007 (bottom row).	
736		Left: MERRA reanalysis. Right: Model.	43
737	Fig. 7.	Spectral density of gravity wave momentum flux at the tropopause in $\text{mPa deg}^{-1} (\text{m/s})^{-1}$	
738		as functions of azimuthal angle from east and phase speed for December 2006 (left) and	
739		December 2007 (right). The spectra are averaged between 15-17 km altitude.	44
740	Fig. 8.	Zonal gravity wave momentum fluxes (mPa/ms^{-1}) at the tropopause for Dec 2006 (red) and	
741		Dec 2007 (blue).	45
742	Fig. 9.	Regional variations in the gravity wave momentum flux spectrum December 2006. (a) Map	
743		of the 400hPa latent heating ($0\text{-}1 \text{ K hr}^{-1}$) shown for reference, with dashed lines marking	
744		each latitude/longitude sector. (b) Nine different azimuth (W-S-E-N-W) vs. phase speed	
745		($0\text{-}32 \text{ m s}^{-1}$) momentum flux spectra, one for each sector. (c) Equatorial 100hPa zonal wind	
746		(red, left axis) and momentum flux (symbols, right axis). Blue background marks westward	
747		winds, and pink marks eastward winds.	46
748	Fig. 10.	Regional variations in the gravity wave momentum flux spectrum December 2007. (a) Map	
749		of the 400hPa latent heating ($0\text{-}1 \text{ K hr}^{-1}$) shown for reference, with dashed lines marking	
750		each latitude/longitude sector. (b) Nine different azimuth (W-S-E-N-W) vs. phase speed	
751		($0\text{-}32 \text{ m s}^{-1}$) momentum flux spectra, below each sector. (c) Equatorial 100hPa zonal wind	
752		(blue, left axis) and momentum flux (symbols, right axis). Blue background marks westward	
753		winds, and pink marks eastward winds.	47
754	Fig. 11.	Tropical (20S - 20N) momentum flux distributions for Dec 2006 (red) and Dec 2007 (blue).	
755		(a) Distributions at 20 km. The black line shows the distribution derived from limb-sounding	
756		satellite observations (HIRDLS/COSMIC [Alexander 2015]) for Dec 2006-Dec 2007. (b)	
757		Distributions from the model at 17 km.	48
758	Fig. 12.	(a) Dec 2006 zonal wavenumber-frequency spectrum of vertical Eliassen-Palm flux (F_Z) at	
759		20 km with the small box near the origin indicating planetary-scale waves with frequencies	

$<1 \text{ cyc d}^{-1}$ and zonal wavenumbers <12 . (b) Dec 2006 profiles of integrated F_Z divergence (force). Two black and two red profiles show spectra integrated separately over positive and negative wavenumbers, with positive and negative values respectively. Black profiles show the result from integrating the total spectrum while red show the integration only over the planetary-scale waves. (c) Same as (a) but for Dec 2007. (d) Same as (b) but for Dec 2007. . . . 49

Fig. A1. Profiles of latent heating averaged over land (solid) and ocean (dashed). Left: December 2006. Right: December 2007. 50



767 FIG. 1. Example snapshots of $0.25^\circ \times 0.25^\circ$ resolution rain rates (left) and cloud top heights (right) at 03:00
 768 UT on 1 Dec 2006.



769 FIG. 2. Left: Time series of the monthly ENSO 3.4 sea surface temperature anomaly showing December 2006
 770 and December 2007 as weak El Niño ($>+1^{\circ}$) and moderate La Niña ($<-1.5^{\circ}$) events, respectively. (Data source:
 771 NOAA/ESRL/PSD.) Center: MJO index (top) and phase (bottom) for Dec 2006 (red) and Dec 2007 (blue) as
 772 defined by the MJO Multivariate Index [Wheeler and Hendon, 2004]. Right: Wind profiles for Dec 2006 (red)
 773 and Dec 2007 (blue).

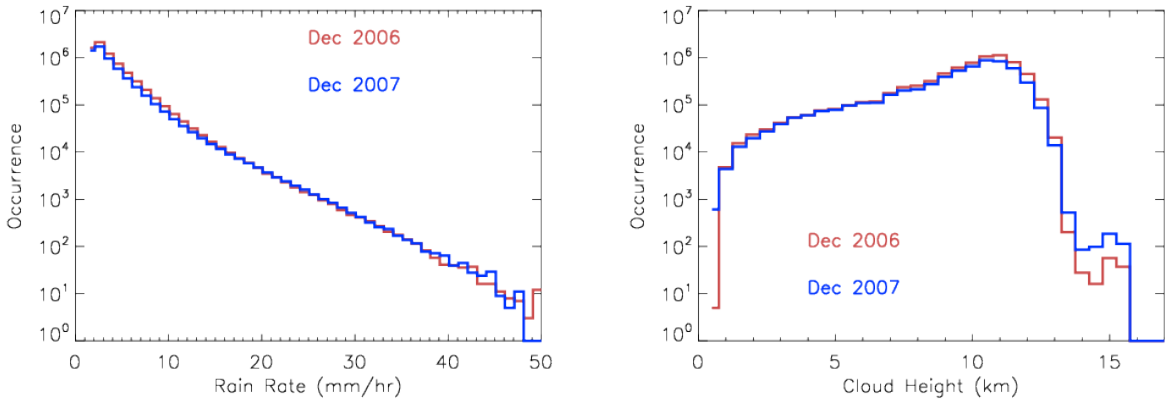
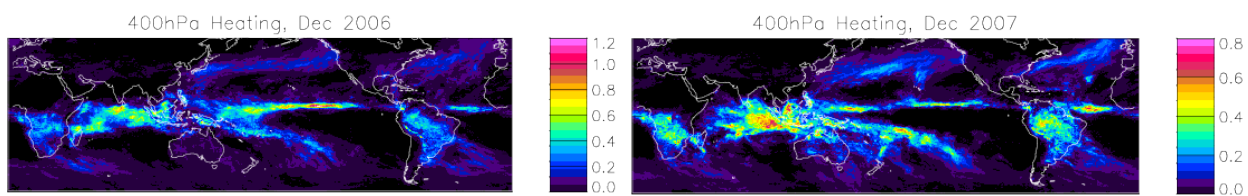
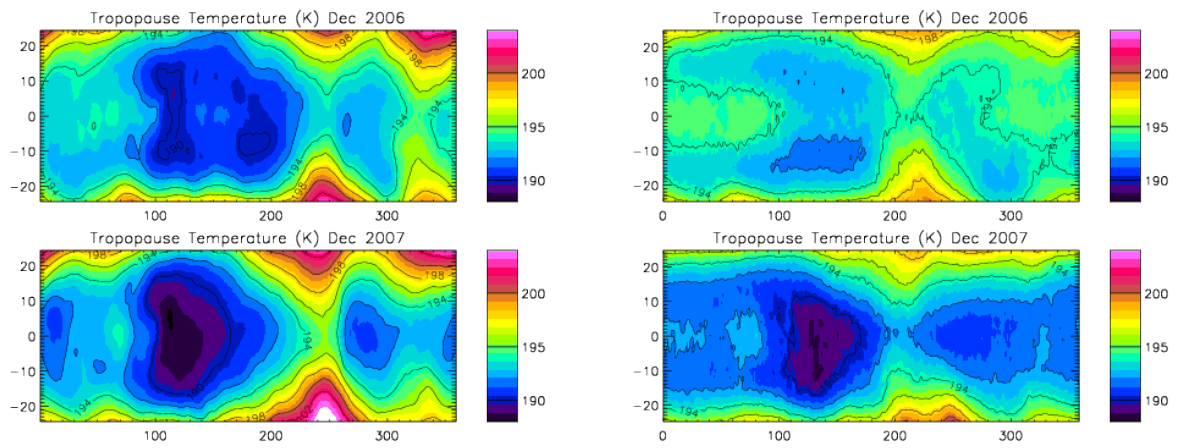


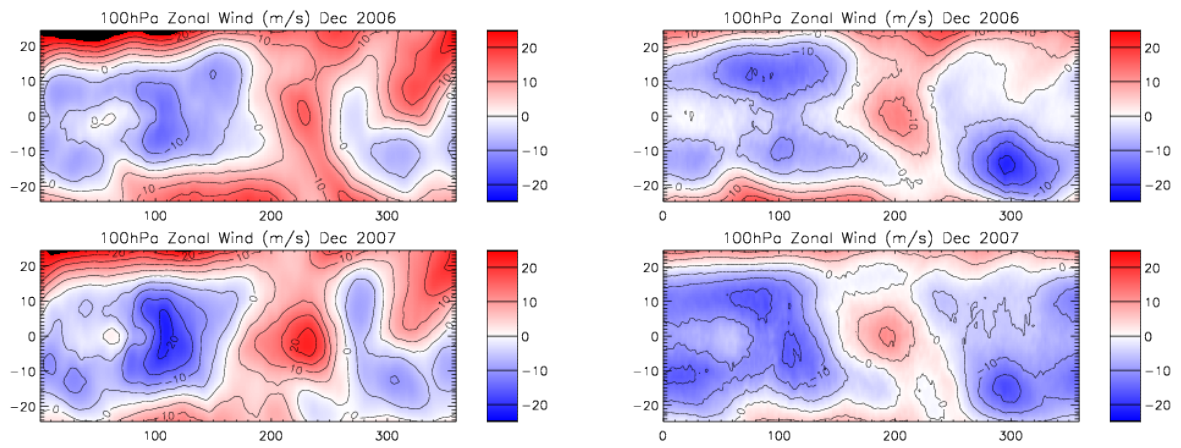
FIG. 3. Distributions of tropical 10°S-10°N rain rates (left) and cloud top heights (right) at $0.25^\circ \times 0.25^\circ$ resolution for “convective rain” points, those with rates exceeding 1.6 mm hr^{-1} . Colors indicate Dec 2006 (red) and Dec 2007 (blue).



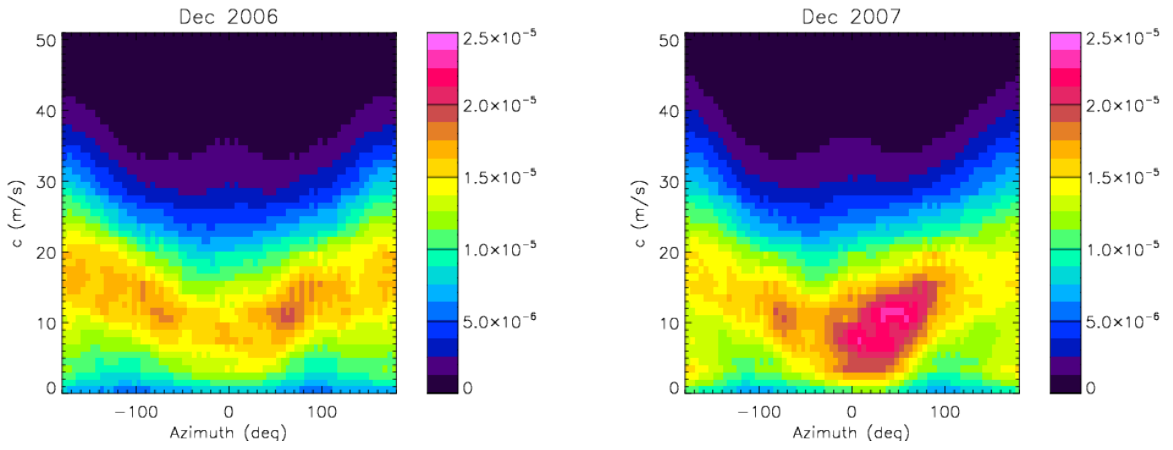
777 FIG. 4. Monthly-averaged 400 hPa latent heating (K hr^{-1}) mapped 60°S - 60°N for December 2006 (left) and
 778 December 2007 (right) shown at $0.25^\circ \times 0.25^\circ$ resolution. The patterns illustrate typical ENSO variability.



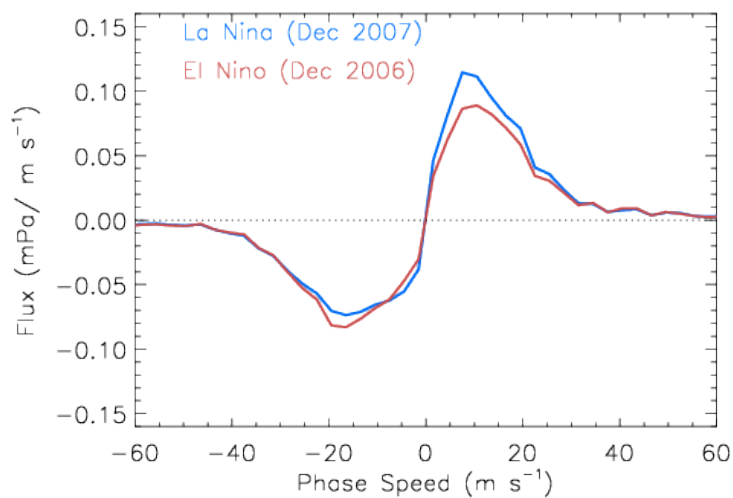
779 FIG. 5. Monthly-mean tropopause temperatures for Dec 2006 (top row) and Dec 2007 (bottom row). Left:
 780 MERRA reanalysis. Right: Model.



781 FIG. 6. Monthly-mean 100hPa zonal winds for Dec 2006 (top row) and Dec 2007 (bottom row). Left:
 782 MERRA reanalysis. Right: Model.



783 FIG. 7. Spectral density of gravity wave momentum flux at the tropopause in $\text{mPa deg}^{-1} (\text{m/s})^{-1}$ as functions
 784 of azimuthal angle from east and phase speed for December 2006 (left) and December 2007 (right). The spectra
 785 are averaged between 15-17 km altitude.



786 FIG. 8. Zonal gravity wave momentum fluxes (mPa/ms^{-1}) at the tropopause for Dec 2006 (red) and Dec 2007
787 (blue).

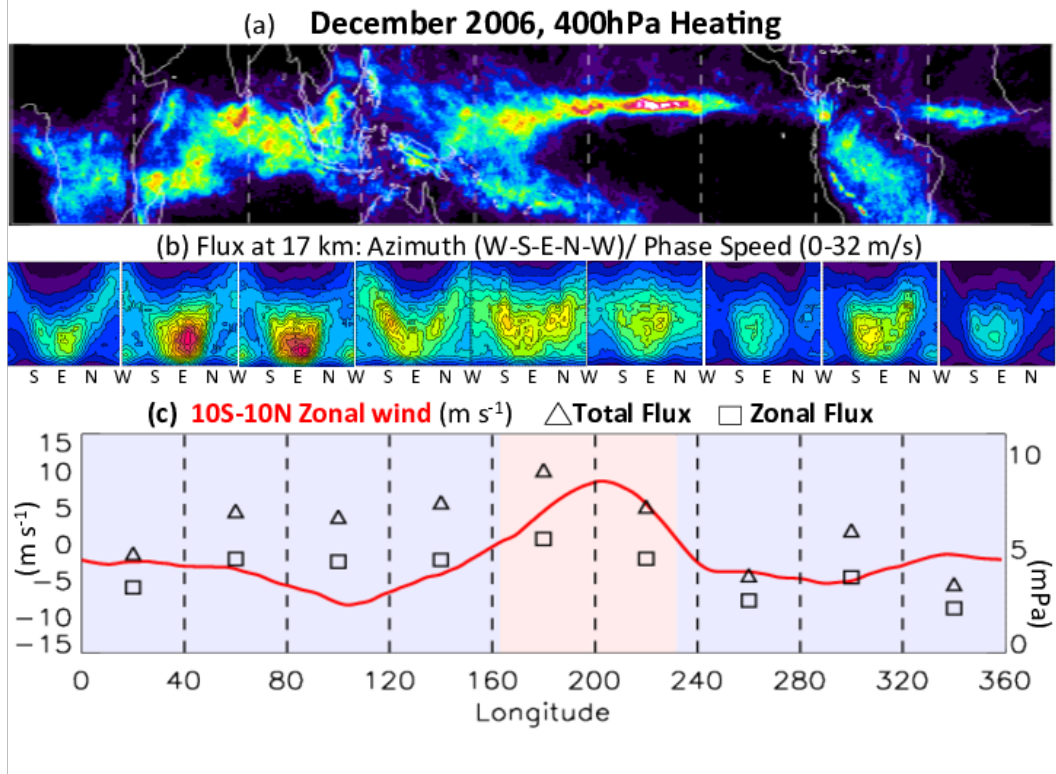


FIG. 9. Regional variations in the gravity wave momentum flux spectrum December 2006. (a) Map of the 400hPa latent heating ($0-1 \text{ K hr}^{-1}$) shown for reference, with dashed lines marking each latitude/longitude sector. (b) Nine different azimuth (W-S-E-N-W) vs. phase speed ($0-32 \text{ m s}^{-1}$) momentum flux spectra, one for each sector. (c) Equatorial 100hPa zonal wind (red, left axis) and momentum flux (symbols, right axis). Blue background marks westward winds, and pink marks eastward winds.

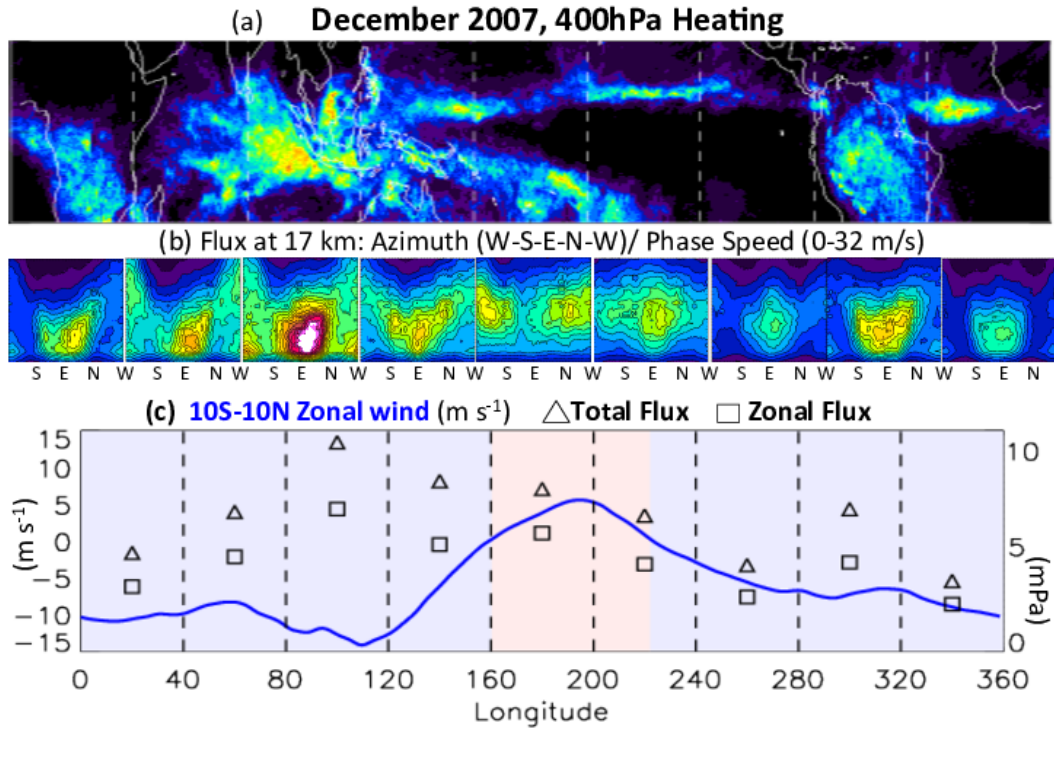
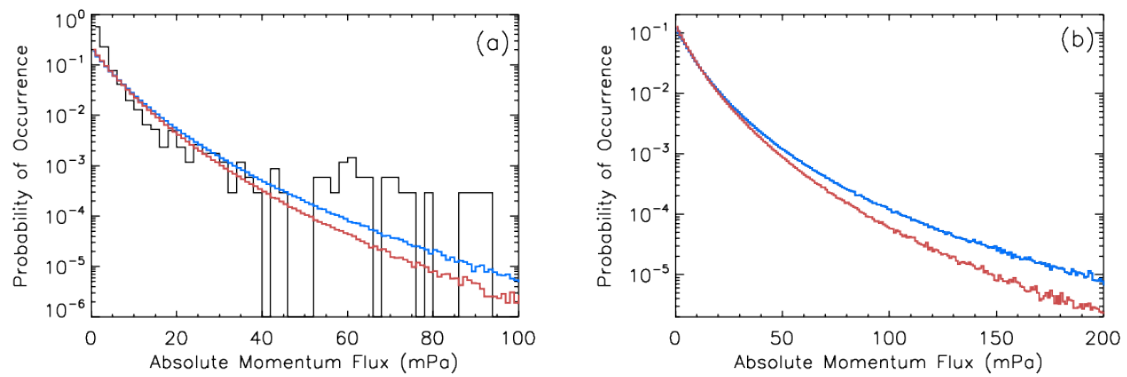


FIG. 10. Regional variations in the gravity wave momentum flux spectrum December 2007. (a) Map of the 400hPa latent heating ($0-1 \text{ K hr}^{-1}$) shown for reference, with dashed lines marking each latitude/longitude sector. (b) Nine different azimuth (W-S-E-N-W) vs. phase speed ($0-32 \text{ m s}^{-1}$) momentum flux spectra, below each sector. (c) Equatorial 100hPa zonal wind (blue, left axis) and momentum flux (symbols, right axis). Blue background marks westward winds, and pink marks eastward winds.



798 FIG. 11. Tropical (20S-20N) momentum flux distributions for Dec 2006 (red) and Dec 2007 (blue). (a)
 799 Distributions at 20 km. The black line shows the distribution derived from limb-sounding satellite observations
 800 (HIRDLs/COSMIC [Alexander 2015]) for Dec 2006-Dec 2007. (b) Distributions from the model at 17 km.

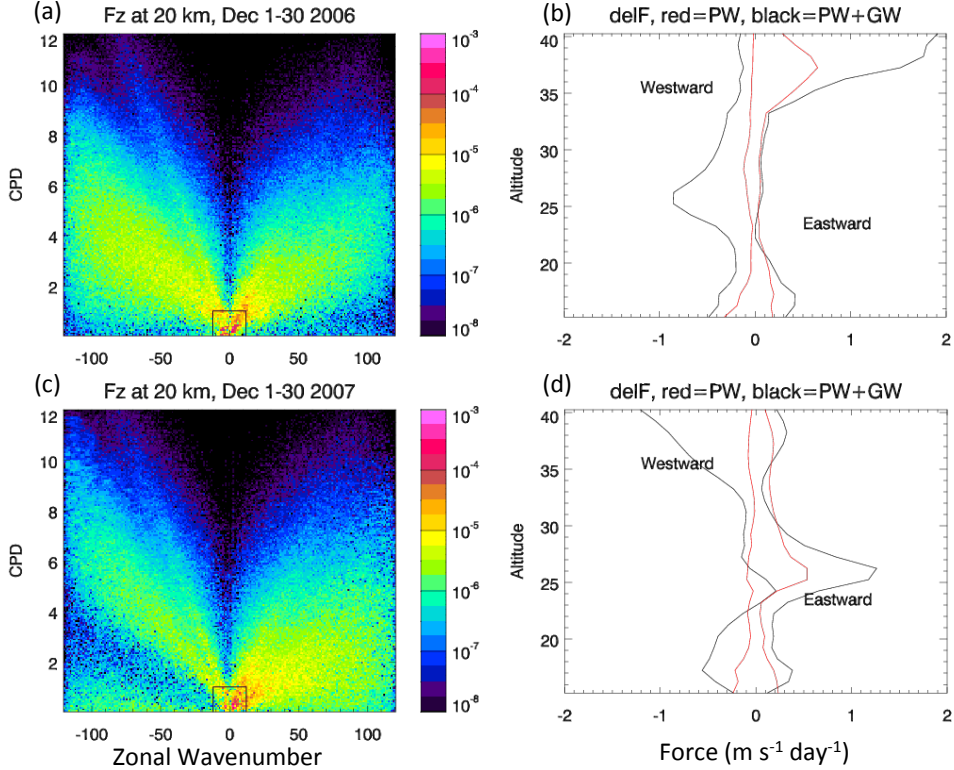


FIG. 12. (a) Dec 2006 zonal wavenumber-frequency spectrum of vertical Eliassen-Palm flux (F_Z) at 20 km with the small box near the origin indicating planetary-scale waves with frequencies <1 cyc d^{-1} and zonal wavenumbers <12 . (b) Dec 2006 profiles of integrated F_Z divergence (force). Two black and two red profiles show spectra integrated separately over positive and negative wavenumbers, with positive and negative values respectively. Black profiles show the result from integrating the total spectrum while red show the integration only over the planetary-scale waves. (c) Same as (a) but for Dec 2007. (d) Same as (b) but for Dec 2007.

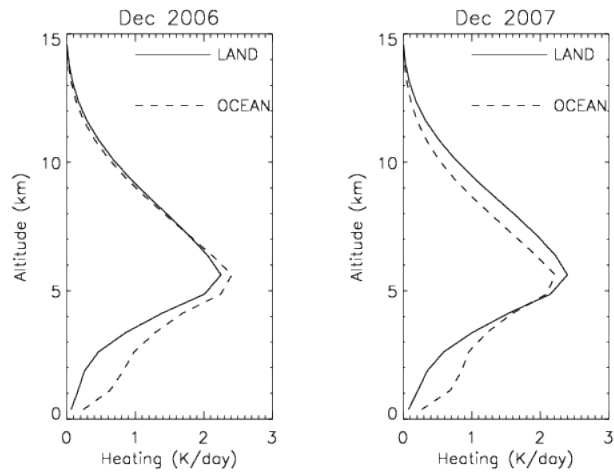


Fig. A1. Profiles of latent heating averaged over land (solid) and ocean (dashed). Left: December 2006.
Right: December 2007.